Journal of Power Sources 185 (2008) 55–62

Contents lists available at ScienceDirect

Journal of Power Sources

journal homepage: www.elsevier.com/locate/jpowsour

Analyzing the effects of immobile liquid saturation and spatial wettability variation on liquid water transport in diffusion media of polymer electrolyte fuel cells (PEFCs)

Hyunchul Ju*

School of Mechanical Engineering, Inha University, 253 Yonghyun-Dong, Nam-Gu, Incheon 402-751, Republic of Korea

ARTICLE INFO

Article history:
Received 7 April 2008
Received in revised form 26 May 2008
Accepted 13 June 2008
Available online 10 July 2008

Keywords:
Fuel cell
Diffusion media
Immobile liquid saturation
Two-phase transport
Wettability

ABSTRACT

Capillary-induced transport of liquid water inside the porous diffusion media (DM) of polymer electrolyte fuel cells (PEFCs) is strongly dependent on DM pore structure and material properties. As such, excessive liquid in the DM can be expelled more efficiently into flow channels by proper design of the DM structure. The present study is devoted to exploring multiphase transport characteristics by considering the effects of DM pore structure and material properties. Two main effects on overall water removability are examined, namely: (i) the effect of immobile liquid saturation, which is a threshold value for initiating macroscopic capillary transport via connected small liquid droplets, and (ii) the effect of hydrophobic spatial variation, which is encountered in typical DM treated with PTFE. Although these two effects are expected to influence significantly the transport characteristics in the fuel cell DM, they have been ignored in most two-phase fuel cell models reported in the literature. In the present work, these features are implemented into a one-dimensional, multiphase mixture (M^2) fuel cell model along the through-plane direction, where both anode and cathode sides and the membrane are fully incorporated. The results of the model simulation clearly demonstrate the dramatic influence of the amount of liquid accumulation and capillary transport characteristics inside the DM. The findings are useful for designing and optimizing DM for the purpose of effective water removal.

1. Introduction

Water management in polymer electrolyte fuel cells (PEFCs) affects performance, durability, and cold-start characteristics. Diffusion media (DM) in PEFCs should be able to expel efficiently excessive water condensed in the catalyst layer (CL) into the flow channels in order to minimize flooding. Typical carbon–fibre-based DM are a carbon-fiber-based porous materials treated with PTFE, and display complex pore structures and non-uniform wetting characteristics [1–3]. Accordingly, DM pore structure and material properties are key factors for the control of liquid water transport in the DM and thus need to be optimized for better water management of PEFCs.

Two-phase transport and resulting flooding phenomena in DM have been investigated using both modelling and experimental studies. A large number of macroscopic PEFC models reported in the literature are based on the two-phase Darcy's law under for a homogeneous pore structure and uniform wetting characteristics [4–22]. Some publications further analyze the effects of a micro porous layer (MPL), which is finer and more hydrophobic than traditional DM [18–21]. Although macroscopic fuel cell models are based on descriptions of continuous flow and transport, the effect of immobile liquid saturation, which constitutes a threshold for a continuous liquid phase, has been largely ignored. Only a few researchers [20–22] have examined its influence on the amount of liquid accumulation in DM.

Simultaneously, efforts have also been made to investigate experimentally the effects of DM pore structure and hydrophobicity on water transport through DM as well as on cell performance. Kong et al. [23] showed the influence of DM pore-size distribution on cell *I–V* performance curves. Park et al. [24] and Qi and Kaufman [25] compared and analyzed cell performance using DM with different pore structures, PTFE contents, and MPLs. In addition, a neutron radiography technique was employed to examine the effect of DM properties on liquid accumulation in PEFCs [26–28]. These experimental studies provide strong evidence that DM structure and wettability affect water transport characteristics in fuel cell DM.

Macroscopic models have inherent limitations in accurately describing multi-phase flows through heterogeneous porous

* Tel.: +1 82 32 860 7312; fax: +1 82 32 868 1716.
E-mail address: hcju@inha.ac.kr.

0378-7753/$ – see front matter © 2008 Elsevier B.V. All rights reserved.
doi:10.1016/j.jpowsour.2008.06.085

Nomenclature

a	water activity or effective catalyst area per unit of total volume ($m^2\ m^{-3}$)
A	area (m^2)
D_k	mass diffusivity of species k ($m^2\ s^{-1}$)
EW	equivalent weight of dry membrane (kg/mol)
F	Faraday constant (96,487 C mol^{-1})
I	current density ($A\ m^{-2}$)
j^i	diffusive mass flux of i phase ($kg\ m^{-2}\ s^{-1}$)
J	Leverett function
k_r	relative permeability
K	hydraulic permeability (m^2)
m	mass fraction
M	molecular weight ($kg\ mol^{-1}$)
n	number of electrons in electrochemical reaction or diffusivity correction factor
n_d	electroosmotic drag coefficient
P	pressure (Pa)
P_c	capillary pressure (Pa)
RH	inlet relative humidification
R_u	universal gas constant (8.314 J $mol^{-1}\ K^{-1}$)
s	liquid saturation
s_{im}	immobile liquid saturation
s_{int}	interfacial liquid coverage
s_r	reduced liquid saturation
T	temperature (K)
u	fluid velocity and superficial velocity in porous medium ($m\ s^{-1}$)
V	volume (m^3)

Greek letters

α	transfer coefficient
γ	advection correction factor
δ_i	thickness of component i
ε	volume fraction of gaseous phase in porous region
θ	contact angle (°)
λ	membrane water content (mol H_2O/mol SO_3^-)
λ^α	relative mobility of phase α
μ	viscosity ($kg\ m^{-1}\ s^{-1}$)
ρ	density ($kg\ m^{-3}$)
ρ^{mem}	dry membrane density ($kg\ m^{-3}$)
σ	surface tension ($N\ m^{-1}$) or electronic conductivity ($S\ m^{-1}$)
τ	viscous shear stress ($N\ m^{-2}$)
υ	kinematic viscosity ($m^2\ s^{-1}$)

Subscripts

a	anode
avg	average value
c	cathode
CL	catalyst layer
DM	diffusion medium
g	gas phase
GC	gas channel
H_2	hydrogen
i	species index
mem	membrane
N_2	nitrogen
O_2	oxygen
sat	saturation value
w	water
0	standard condition, 298.15 K and 101.3 kPa (1 atm.)

Superscripts

eff	effective value in porous region
mem	membrane
g	gas
l	liquid
sat	saturation value

media. In response to this, pore-scale modelling and simulations have recently been conducted by several fuel cell research groups, with the aim of more precisely investigating the liquid water transport mechanism through a fibrous DM structure [29–34]. In addition to providing constitutive relations under a carbon–fibre-based DM microstructure (e.g., capillary pressure and relative permeability as a function of liquid saturation), which are employed as inputs for macroscopic two-phase fuel cell models, the pore-level simulations revealed that pore morphology and non-uniform spatial distribution of wettability strongly influence the capillary transport characteristics and liquid water accumulation inside DM. While pore-level models are capable of predicting more realistic liquid water profiles, these models are computationally more demanding compared with macroscopic models based on the volume averaging theory. Furthermore, they are more difficult to incorporate into a comprehensive fuel cell model.

In the present work, we describe the effects of immobile liquid saturation and non-uniform DM wettability using macroscopic two-phase fuel cell simulations. These features are implemented into a two-phase PEFC model. The model is a one-dimensional, multiphase mixture (M^2) fuel cell model along the through-plane direction that fully incorporates both the anode and cathode sides and the membrane. Model simulations and analyses yield a better macroscopic understanding of two-phase transport processes and flooding physics. This provides useful information in designing and optimizing DM for the purpose of effective water removal.

2. Two-phase PEFC model

2.1. Multi-phase mixture (M^2) model

The one-dimensional, two-phase flow model presented in the current study is based on a percolation theory proposed by Pasaogullari and Wang [4] and Nam and Kaviany [20]. In the theory, liquid water droplets that preferentially occupy larger pores in hydrophobic porous DM can agglomerate and become a continuous liquid phase. The continuous phase enables the liquid water to move through the DM under a liquid pressure gradient. The macroscopic multi-phase flow phenomena through porous media are traditionally modelled by a multiphase mixture (M^2) approach where consideration of immobile liquid saturation is indispensable for the description of continuous flow and transport. In the present study, a previously described M^2-based fuel cell model [4,5,12,18] is reformulated by adding a new feature, namely, immobile liquid saturation.

In order to quantify individual phase distributions in porous media, liquid saturation, s, is defined as the volume fraction of pores occupied by the liquid phase:

$$s = \frac{V^l}{V} \tag{1}$$

When the immobile liquid saturation, s_{im}, is taken into account, a reduced liquid saturation, s_r, which can be interpreted as the

fraction of transportable liquid, has to be introduced as follows:

$$s_r = \frac{s - s_{im}}{1 - s_{im}} \tag{2}$$

Since two-phase transport inside porous DM is mainly governed by capillary motion between liquid and gas phases, capillary pressure, defined as the difference between gas and liquid pressures, is a basic parameter in the M^2 model. The capillary pressure, P_c, is expressed as [35]:

$$P_c = P^g - P^l = \sigma \cos\theta \left(\frac{\varepsilon}{K}\right)^{1/2} J(s_r) \tag{3}$$

where ε, K, and θ are the porosity, the permeability, and the contact angle of the given porous media, respectively. In Eq. (3), the Leverett function, $J(s_r)$, meaning a dimensionless capillary pressure, can be expressed as a function of the reduced liquid saturation, s_r, for the given hydrophobic DM:

$$J(s_r) = \begin{cases} 0 & \text{if } s \le s_{im} \\ 1.417 s_r - 2.120 s_r^2 + 1.263 s_r^3 & \text{if } s > s_{im} \end{cases} \tag{4}$$

It should be noted here that the standard Leverett J-function form in Eq. (4) was formulated to characterize the liquid transport in more uniform porous media such as soils and rocks [36,37]. A more realistic capillary pressure–saturation study for real fuel cell DM was recently conducted by Gostick et al. [3] and Kumbur et al. [2,39,38]. In particular, Kumbur et al. [39] conducted capillary pressure–saturation measurements under typical fuel-cell compressed DM and operating temperatures (20, 50, and 80 °C). Experimental measurements were compared with capillary pressure–saturation correlation test data obtained with the traditional Leverett function. According to the comparison, the deviation between the Leverett function and new correlations was not significant, especially for the practical range of liquid saturation ($0 < s < 0.5$) in DM during fuel cell operation. Therefore, we have employed the standard Leverett J-function, i.e., Eq. (4), in this study.

On the other hand, a relative permeability term should be introduced for the two-phase porous region because the available pore space in porous DM is shared by both gas and liquid phases. The relative permeability for an individual phase can also be expressed in terms of reduced liquid saturation, s_r, as follows:

$$k_r^l = \begin{cases} 0 & \text{if } 0 \le s \le s_{im} \\ {s_r}^3 = \left(\dfrac{s - s_{im}}{1 - s_{im}}\right)^3 & \text{if } s > s_{im} \end{cases} \tag{5a}$$

$$k_r^g = (1 - s)^3 \tag{5b}$$

where k_r^l and k_r^g denote the relative permeabilities of non-wetting liquid and wetting gas phases, respectively, for hydrophobic DM. Fig. 1 schematically shows the relative permeability curves as a function of liquid saturation, s, as defined in Eq. (1). It is seen that the relative permeability of the non-wetting liquid phase, k_r^l is zero until liquid saturation, s exceeds the threshold value at immobile liquid saturation.

Finally, all mixture properties in the M^2 formulation are defined as follows [35].

Mixture density:

$$\rho = \rho^l s + \rho^g (1 - s) \tag{6}$$

where the gas mixture density, ρ^g, described by the ideal gas law varies with its composition (mass fractions, m_i^g). That is,

$$\rho^g = \left(\frac{P}{R_u T}\right) \frac{1}{\sum_i m_i^g / M_i} \tag{7}$$

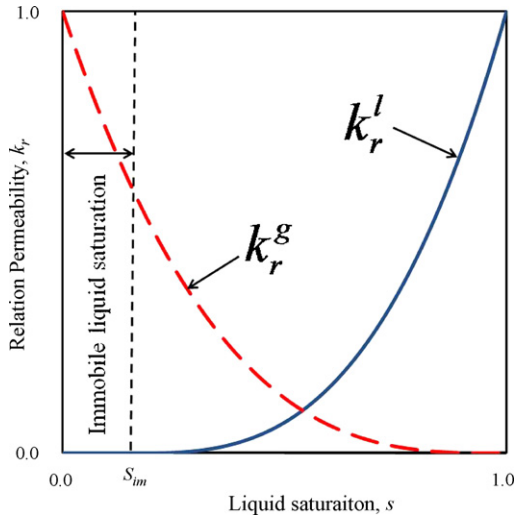

Fig. 1. Relative permeabilities for non-wetting liquid and wetting gas phases as function of liquid saturation for hydrophobic DM. Dashed line denotes immobile liquid saturation.

Mixture velocity:

$$u = \frac{\rho^l u^l + \rho^g u^g}{\rho} \tag{8}$$

Species mass fraction:

$$m_i = \frac{\rho^l s m_i^l + \rho^g (1 - s) m_i^g}{\rho} \tag{8}$$

Kinematic viscosity:

$$\upsilon = \left(\frac{k_r^l}{\nu^l} + \frac{k_r^g}{\nu^g}\right)^{-1} \tag{9}$$

where ν^g is the kinematic viscosity of a gas mixture varying with gas composition [40]:

$$\upsilon^g = \frac{\mu^g}{\rho^g} = \frac{1}{\rho^g} \sum_{i=1}^{n} \frac{x_i \mu_i}{\sum_{j=1}^{n} x_j \Phi_{ij}},$$

$$\text{where } \Phi_{ij} = \frac{1}{\sqrt{8}} \left(1 + \frac{M_i}{M_j}\right)^{-1/2} \left[1 + \left(\frac{\mu_i}{\mu_j}\right)^{1/2} \left(\frac{M_j}{M_i}\right)^{1/4}\right] \tag{10}$$

and

$$\mu_i \ (\mathrm{N\,s/m^2}) = \begin{cases} \mu_{H_2} = 0.21 \times 10^{-6} T^{0.66} \\ \mu_w = 0.00584 \times 10^{-6} T^{1.29} \\ \mu_{N_2} = 0.237 \times 10^{-6} T^{0.76} \\ \mu_{O_2} = 0.246 \times 10^{-6} T^{0.78} \end{cases}, \quad T \text{ in K}$$

Relative mobility:

$$\lambda^l = \frac{k_r^l}{\nu^l} \nu \tag{11}$$

$$\lambda^g = 1 - \lambda^l \tag{12}$$

2.2. Fuel cell model description and assumptions

In this study, for complicity, the computational domain is confined to the anode DM, the catalyst coated membrane (CCM) and the cathode DM. Therefore, both the anode and cathode gas channels (GCs) are excluded from the computational domain by applying proper boundary conditions to the DM|GC interfaces. In addition,

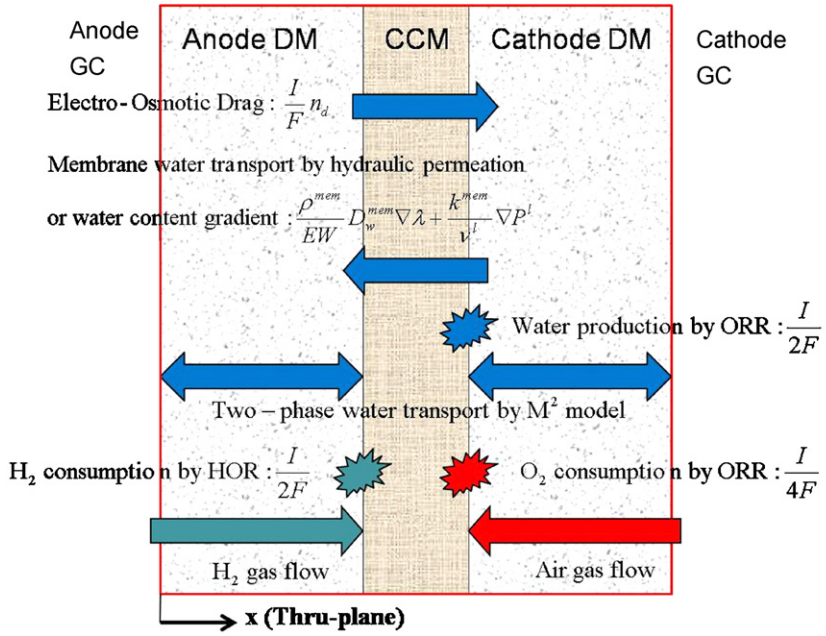

Fig. 2. Schematic of modelling domain and transport phenomena, where HOR and ORR denote hydrogen oxidation reaction in anode side and oxygen reduction reaction in the cathode side, respectively.

the cell is assumed to be under steady-state and isothermal conditions in order to simplify numerical analysis and emphasize liquid water formation. The schematic diagram presented in Fig. 2 depicts the associated transport processes in this model.

2.3. Conservation equations

Mass conservation in steady-state along the through-plane direction (x) is

$$\frac{\mathrm{d}}{\mathrm{d}x}(\rho u) = 0 \tag{13}$$

If Eq. (13) is integrated along the x direction, the total mass flux through the porous DM is given by the following relationship.

Mass transport in the anode DM:

$$\rho u = \frac{I}{2F}M_{\mathrm{H_2}} + \left[n_{\mathrm{d}}\frac{I}{F} - D_{\mathrm{w}}^{\mathrm{mem}}\frac{\rho^{\mathrm{mem}}}{\mathrm{EW}}\left(\frac{\mathrm{d}\lambda}{\mathrm{d}x}\right)_{\mathrm{mem}}\right]M_{\mathrm{w}} - \frac{K^{\mathrm{mem}}}{\nu^{\mathrm{l}}}\frac{\mathrm{d}P^{\mathrm{l}}}{\mathrm{d}x}\Bigg)_{\mathrm{mem}} \tag{14}$$

Mass transport in the cathode DM:

$$\rho u = -\frac{I}{4F}M_{\mathrm{O_2}} + \frac{I}{2F}M_{\mathrm{w}} + \left[\left(n_{\mathrm{d}}+\frac{1}{2}\right)\frac{I}{F} - D_{\mathrm{w}}^{\mathrm{mem}}\frac{\rho^{\mathrm{mem}}}{\mathrm{EW}}\left(\frac{\mathrm{d}\lambda}{\mathrm{d}x}\right)_{\mathrm{mem}}\right]M_{\mathrm{w}} - \frac{K^{\mathrm{mem}}}{\nu^{\mathrm{l}}}\frac{\mathrm{d}P^{\mathrm{l}}}{\mathrm{d}x}\Bigg)_{\mathrm{mem}} \tag{15}$$

where the terms on the right-hand side of Eqs. (14) and (15) represent the reactants and product fluxes due to the electrochemical reactions and water flux across the membrane that is driven by the hydraulic pressure gradient, diffusion due to the water content gradient, and electro-osmotic drag due to proton flux (see Fig. 2).

For the momentum conservation equations for flow through the porous DM, Darcy's law is used instead Navier–Stokes equations. For the two-phase region, the Darcy's equations are derived according to the M^2 model for both single- and two-phase porous regimes. The equation can be written in one-dimensional form as

$$\rho u = \frac{K}{\nu}\frac{\mathrm{d}P}{\mathrm{d}x} \tag{16}$$

The steady-state, one-dimensional species conservation equation can be written as [35]:

$$\frac{\mathrm{d}}{\mathrm{d}x}(\gamma_i \rho m_i u) = \frac{\mathrm{d}}{\mathrm{d}x}\left[\rho^{\mathrm{g}} D_i^{\mathrm{g,eff}}\frac{\mathrm{d}}{\mathrm{d}x}(m_i^{\mathrm{g}})\right] + \frac{\mathrm{d}}{\mathrm{d}x}[(m_i^{\mathrm{g}} - m_i^{\mathrm{l}})j^{\mathrm{l}}] \tag{17}$$

where j^{l} in the second term on the right-hand side of Eq. (17) denotes the diffusive mass flux of liquid phase relative to the whole multiphase mixture [35]. It can be expressed in a one-dimensional form as follows:

$$j^{\mathrm{l}} = \rho^{\mathrm{l}}u^{\mathrm{l}} - \lambda^{\mathrm{l}}\rho u \tag{18}$$

On the other hand, the term on the left-hand side of Eq. (17) represents the advective term, where the advection correction factor, γ_i is given by [35]:

$$\gamma_i = \frac{\rho(\lambda^{\mathrm{l}}m_i^{\mathrm{l}} + \lambda^{\mathrm{g}}m_i^{\mathrm{g}})}{(s\rho^{\mathrm{l}}m_i^{\mathrm{l}} + (1-s)\rho^{\mathrm{g}}m_i^{\mathrm{g}})} \tag{19}$$

Species diffusivity in the gas mixture, D_i^{g}, in the first term on the right-hand side of Eq. (17), is defined such that summation of inter-species diffusion within the gas phase will be equal to zero [40]:

$$D_i^{\mathrm{g}} = \frac{1-x_i}{\sum_{\substack{j\\ j\neq i}}^{j=n} x_j/D_{i,j}},$$

$$\text{where } D_{i,j} = \frac{1.013\times10^{-7}T^{1.75}}{p\left(\chi_i^{1/3}+\chi_j^{1/3}\right)^2}\left(\frac{1}{M_i}+\frac{1}{M_j}\right)^{1/2},$$

$$\chi_{\mathrm{H_w}} = 7.07,\quad \chi_{\mathrm{w}} = 12.7,\quad \chi_{\mathrm{N_w}} = 17.9,\quad \chi_{\mathrm{O_w}} = 16.6 \tag{20}$$

Note that gaseous diffusive transport for a porous medium can be controlled by the Knudsen diffusion effect due to molecule-to-wall collisions, as well as molecular diffusion caused by molecular col-

lisions, as described in Eq. (20). The Knudsen diffusion coefficient can be computed according to the kinetic theory of gases as follows:

$$D_i^{\mathrm{K}} = \frac{2}{3}\left(\frac{8R_{\mathrm{u}}T}{\pi M_i}\right)^{1/2} r_{\mathrm{p}} \tag{21}$$

The effective diffusivity of species, i in the gas mixture, is then obtained by combining both molecular and Knudsen diffusion effects with the effects of porosity and tortuosity of the porous medium by means of the Bruggeman correlation [41]:

$$D_i^{\mathrm{g,eff}} = [\varepsilon(1-s)]^n \left(\frac{1}{D_i^{\mathrm{g}}} + \frac{1}{D_i^{\mathrm{K}}}\right)^{-1} \tag{22}$$

where it is seen that the effective gas diffusivity $D_i^{\mathrm{g,eff}}$ in the two-phase region is a function of both the porosity, ε, and the liquid saturation, s.

Eq. (17) can be written for water species as

$$\frac{\mathrm{d}}{\mathrm{d}x}(\gamma_{\mathrm{w}}\rho m_{\mathrm{w}}u) = \frac{\mathrm{d}}{\mathrm{d}x}\left[\rho^{\mathrm{g}} D_{\mathrm{w}}^{\mathrm{g,eff}} \frac{\mathrm{d}}{\mathrm{d}x}(m_{\mathrm{w}}^{\mathrm{g}})\right] + \frac{\mathrm{d}}{\mathrm{d}x}[(m_{\mathrm{w}}^{\mathrm{g}} - m_{\mathrm{w}}^{\mathrm{l}})j^{\mathrm{l}}] \tag{23}$$

Again, this equation is integrated over the porous DM to give:

water transport in the anode DM:

$$\gamma_{\mathrm{w}}\rho m_{\mathrm{w}}u = \rho^{\mathrm{g}} D_{\mathrm{w}}^{\mathrm{g,eff}} \frac{\mathrm{d}}{\mathrm{d}x}(m_{\mathrm{w}}^{\mathrm{g}}) + (m_{\mathrm{w}}^{\mathrm{g}} - m_{\mathrm{w}}^{\mathrm{l}})j^{\mathrm{l}} + \left[n_{\mathrm{d}}\frac{I}{F} - D_{\mathrm{w}}^{\mathrm{mem}}\frac{\rho^{\mathrm{mem}}}{\mathrm{EW}}\left(\frac{\mathrm{d}\lambda}{\mathrm{d}x}\right)_{\mathrm{mem}}\right] M_{\mathrm{w}} - \frac{K^{\mathrm{mem}}}{\nu^{\mathrm{l}}}\frac{\mathrm{d}P^{\mathrm{l}}}{\mathrm{d}x}\Bigg)_{\mathrm{mem}} \tag{24}$$

water transport in the cathode DM:

$$\gamma_{\mathrm{w}}\rho m_{\mathrm{w}}u = \rho^{\mathrm{g}} D_{\mathrm{w}}^{\mathrm{g,eff}} \frac{\mathrm{d}}{\mathrm{d}x}(m_{\mathrm{w}}^{\mathrm{g}}) + (m_{\mathrm{w}}^{\mathrm{g}} - m_{\mathrm{w}}^{\mathrm{l}})j^{\mathrm{l}} + \left[\left(n_{\mathrm{d}} + \frac{1}{2}\right)\frac{I}{F} - D_{\mathrm{w}}^{\mathrm{mem}}\frac{\rho^{\mathrm{mem}}}{\mathrm{EW}}\left(\frac{\mathrm{d}\lambda}{\mathrm{d}x}\right)_{\mathrm{mem}}\right] M_{\mathrm{w}} - \frac{K^{\mathrm{mem}}}{\nu^{\mathrm{l}}}\frac{\mathrm{d}P^{\mathrm{l}}}{\mathrm{d}x}\Bigg) \tag{25}$$

As noted earlier, this study takes into account the water transport across the electrolyte phase driven by three modes [the hydraulic pressure gradient, the gradient of membrane water content, and the electro-osmotic drag due to proton flux] can be expressed by the following equation:
water transport across membrane:

$$\frac{\mathrm{d}}{\mathrm{d}x}\left(\frac{\rho^{\mathrm{mem}}}{\mathrm{EW}} D_{\mathrm{w}}^{\mathrm{mem}}\frac{\mathrm{d}\lambda}{\mathrm{d}x}\right) M_{\mathrm{w}} - \frac{\mathrm{d}}{\mathrm{d}x}\left(n_{\mathrm{d}}\frac{I}{F}\right) M_{\mathrm{w}} + \frac{\mathrm{d}}{\mathrm{d}x}\left(\frac{K^{\mathrm{mem}}}{\nu^{\mathrm{l}}}\frac{\mathrm{d}P^{\mathrm{l}}}{\mathrm{d}x}\right) = 0 \tag{26}$$

The transport properties of electrolytes are correlated with the water content of the membrane, λ,which is in turn a function of the water activity, a, as follows [42]:

$$a = \frac{C_{\mathrm{w}}^{\mathrm{g}} R_{\mathrm{u}} T}{P_{\mathrm{sat}}} \tag{27}$$

$$\lambda = \begin{cases} \lambda^{\mathrm{g}} = 0.043 + 17.81a - 39.85a^2 + 36.0a^3 & \text{for } 0 < a \le 1 \\ \lambda^{\mathrm{l}} = 22 \end{cases} \tag{28}$$

The electro-osmotic drag coefficient, n_{d}, and the water diffusion coefficient in the membrane, $D_{\mathrm{w}}^{\mathrm{mem}}$ have been described by Zawodzinski et al. [43] and Motupally et al. [44]:

$$n_{\mathrm{d}} = \begin{cases} 1 & \lambda \le \lambda^{\mathrm{g}} \ (a = 1) \\ 2.5 & \lambda = \lambda^{\mathrm{l}} \end{cases} \tag{29}$$

$$D_{\mathrm{w}}^{\mathrm{mem}} = \begin{cases} 3.1\times10^{-7}\lambda\ (\mathrm{e}^{0.28\lambda} - 1)\,\mathrm{e}^{(-2346/T)} & \text{for } 0 < \lambda \le 3 \\ 4.17\times10^{-8}\lambda\ (1 + 161\,\mathrm{e}^{-\lambda})\,\mathrm{e}^{(-2346/T)} & \text{otherwise} \end{cases} \tag{30}$$

Meanwhile, a one-dimensional oxygen species conservation equation provided by the M^2 formulation is obtained from Eq. (17):

$$\frac{\mathrm{d}}{\mathrm{d}x}(\gamma_{\mathrm{O_2}}\rho m_{\mathrm{O_2}}u) = \frac{\mathrm{d}}{\mathrm{d}x}\left[\rho^{\mathrm{g}} D_{\mathrm{O_2}}^{\mathrm{g,eff}}\frac{\mathrm{d}}{\mathrm{d}x}(m_{\mathrm{O_2}}^{\mathrm{g}})\right] + \frac{\mathrm{d}}{\mathrm{d}x}[m_{\mathrm{O_2}}^{\mathrm{g}} j^{\mathrm{l}}] \tag{31}$$

In this study, no oxygen is assumed in the anode side, and hence Eq. (31) can be integrated over the cathode DM to give:
oxygen transport in cathode DM:

$$\gamma_{\mathrm{O_2}}\rho m_{\mathrm{O_2}}u = \rho^{\mathrm{g}} D_{\mathrm{O_2}}^{\mathrm{g,eff}}\frac{\mathrm{d}}{\mathrm{d}x}(m_{\mathrm{O_2}}^{\mathrm{g}}) + m_{\mathrm{O_2}}^{\mathrm{g}} j^{\mathrm{l}} - \frac{I}{4F} M_{\mathrm{O_2}} \tag{32}$$

2.4. Boundary conditions

The aforementioned one-dimensional model requires boundary conditions for water and oxygen species at the GC|DM interfaces. The interfacial mass fractions for oxygen and water species, $m_{i,\mathrm{DM/GC}}$, are determined by the cell operating pressure (P), temperature (T), GC relative humidity ($\mathrm{RH_{GC}}$), and interfacial liquid droplet coverage (s_{int}) due to channel flooding conditions:

$$\begin{aligned} m_{\mathrm{w,DM/GC}}(s_{\mathrm{int}}, \mathrm{RH_{GC}}, T, P) &= \frac{\rho^{\mathrm{l}} s_{\mathrm{int}} + (1 - s_{\mathrm{int}})(P_{\mathrm{w}} M_{\mathrm{w}}/R_{\mathrm{u}}T)}{\rho^{\mathrm{l}} s_{\mathrm{int}} + \rho^{\mathrm{g}}(1 - s_{\mathrm{int}})} \\ &= \frac{\rho^{\mathrm{l}} s_{\mathrm{int}} + (1 - s_{\mathrm{int}})((\mathrm{RH_{GC}} P_{\mathrm{sat}} M_{\mathrm{w}})/R_{\mathrm{u}}T)}{\rho^{\mathrm{l}} s_{\mathrm{int}} + \rho^{\mathrm{g}}(1 - s_{\mathrm{int}})} \end{aligned} \tag{33}$$

$$\begin{aligned} m_{\mathrm{O_2,DM/GC}}(s_{\mathrm{int}}, \mathrm{RH}, T, P) &= \frac{(1 - s_{\mathrm{int}}) M_{\mathrm{O_2}}(P_{\mathrm{O_2}}/R_{\mathrm{u}}T)}{\rho^{\mathrm{l}} s_{\mathrm{int}} + \rho^{\mathrm{g}}(1 - s_{\mathrm{int}})} \\ &= \frac{(1 - s_{\mathrm{int}}) M_{\mathrm{O_2}}(P - P_{\mathrm{w}} - P_{\mathrm{N_2}}/R_{\mathrm{u}}T)}{\rho^{\mathrm{l}} s_{\mathrm{int}} + \rho^{\mathrm{g}}(1 - s_{\mathrm{int}})} \end{aligned} \tag{34}$$

2.5. Numerical procedures

The first-order ordinary differential equations derived in the foregoing section are solved separately in three different regions, i.e., anode DM, CCM, and cathode DM. In order to connect these differential equations for the three domains, an initial estimated value is provided for the water flux across the membrane to set up the interfacial boundary conditions. An iterative procedure is used to improve the initial estimate where the individually calculated interfacial fluxes in adjoining domains should be matched at the interface. The iterations proceed until the relative error falls below the convergence criterion (10^{-7}).

3. Results and discussion

In this study, the aforementioned one-dimensional PEFC model is applied to typical fuel cell geometry. The cell component properties and physical parameters for the one-dimensional simulations are shown in Table 1. It is assumed for all simulation cases that the cell is operated at a constant temperature of 80 °C and a pressure of 1.5 atm., which are typical of practical PEFC stack operations. In addition, in order to focus on the cell flooding phenomena, GC relative humidity ($\mathrm{RH_{GC}}$) is assumed to be unity, which means that the gas stream in the flow channel is fully saturated.

The effect of immobile liquid saturation on the DM liquid water distribution is illustrated in Fig. 3. The five cases shown correspond

Table 1
Material properties and physical parameters

Description	Value
Porosity of DM, ε_{DM}	0.6
Permeability of DM, K_{DM}	1.0×10^{-12} m^2
Thickness of DM, δ_{DM}	0.3 mm
Hydraulic permeability of membrane, K_{mem}	5.0×10^{-20} m^2
Thickness of membrane, δ_{mem}	0.018 mm
Dry membrane density, ρ_{mem}	2000 kg m^{-3}
Equivalent weight of electrolyte in membrane, EW	1.1 kg mol^{-1}
Faraday constant, F	96,487 C mol^{-1}
Universal gas constant, R_u	8.314 J mol K^{-1}
Surface tension, σ	0.0625 N m^{-1}
Liquid water density, ρ^l (80 °C)	972 kg m^{-3}
Liquid water viscosity, μ^l	3.5×10^{-4} N s m^{-2}

to different immobile liquid saturation values that range from 0 to 0.2, where the immobile liquid saturation for each case is assumed to be constant throughout the entire DM, although it is likely to vary in the random fibrous DM. These cases assume no interfacial liquid coverage ($s_{ic} = 0$) at the DM surface. This means that most of the liquid water transported through the DM is evaporated at the interface of the DM and GC. Thus, channel flooding is minimal [12]. It is clearly seen in Fig. 3 that the amount of liquid water accumulation in the cathode DM is strongly influenced by the magnitude of immobile liquid saturation. Without the effect of immobile liquid saturation, i.e., $s_{im} = 0$, the overall liquid saturation, s_{avg}, averaged along the DM thickness is 0.138 (13.8%) and the maximum liquid saturation of 0.158 (15.8%) is predicted to be near the DM|CCM interface. As the immobile liquid saturation increases, both the overall and maximum liquid saturations of the DM increase. When the immobile liquid saturation is assumed to be 0.2, the overall and maximum liquid saturations are predicted to be 0.295 and 0.320, respectively. Generally, the immobile liquid saturation of porous media is increased when the spatial heterogeneity in porous media also increases. Therefore, it can be concluded from Fig. 3 that the level of DM flooding is strongly influenced by the spatial heterogeneity of the DM.

Fig. 4 displays the effect of interfacial liquid coverage on cathode DM liquid saturation profiles, where $s_{ic} = 20\%$ in Cases 2 and 4 means that the 20% of the cathode DM interfacial surface is covered by liquid water droplets. This implies that appreciable channel flooding exists for these cases. Comparing cases 1 and 2 which have no immobile liquid saturation effect, $s_{im} = 0\%$, much higher liquid saturation is predicted in case 2 which causes a large difference in average liquid saturation, s_{avg} ($\Delta s_{avg} = 6.9\%$). This indicates that interfacial coverage has a significant effect if immobile liquid saturation is assumed to be small. On the other hand, when immobile liquid saturation of 10% is considered, the difference in the average liquid saturation between cases 3 and 4 is smaller ($\Delta s_{avg} = 1.6\%$). The comparison of the four curves pre-

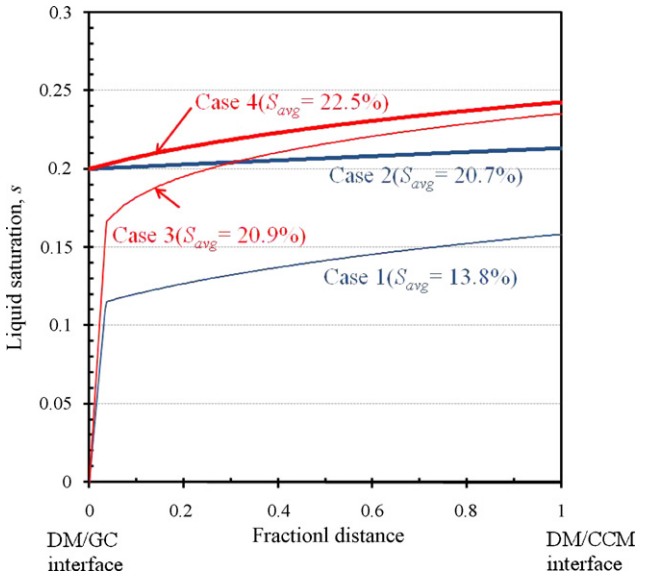

Fig. 4. Liquid saturation profiles in cathode DM with different immobile liquid saturation, s_{im}, interfacial liquid coverage, s_{ic} ($I = 1.5$ A cm^{-2}, DM contact angle, $\theta = 110°$). Case 1: $s_{im} = 0\%$ and $s_{ic} = 0\%$; case 2: $s_{im} = 0\%$ and $s_{ic} = 20\%$; case 3: $s_{im} = 10\%$ and $s_{ic} = 0\%$; case 4: $s_{im} = 10\%$ and $s_{ic} = 20\%$.

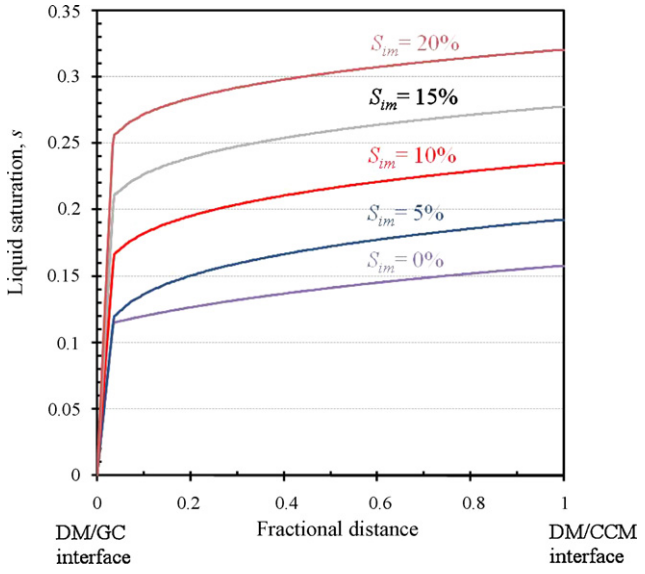

Fig. 3. Liquid saturation profiles in cathode DM as function of immobile liquid saturation, s_{im} ($I = 1.5$ A cm^{-2}, DM contact angle, $\theta = 110°$, $s_{ic} = 0$ for all cases). Overall liquid saturations, s_{avg}, i.e., averaged along DM thickness for cases of $s_{im} = 0.0$, 0.05, 0.10, 0.15, and 0.20 are 0.138, 0.166, 0.209, 0.252, and 0.295, respectively.

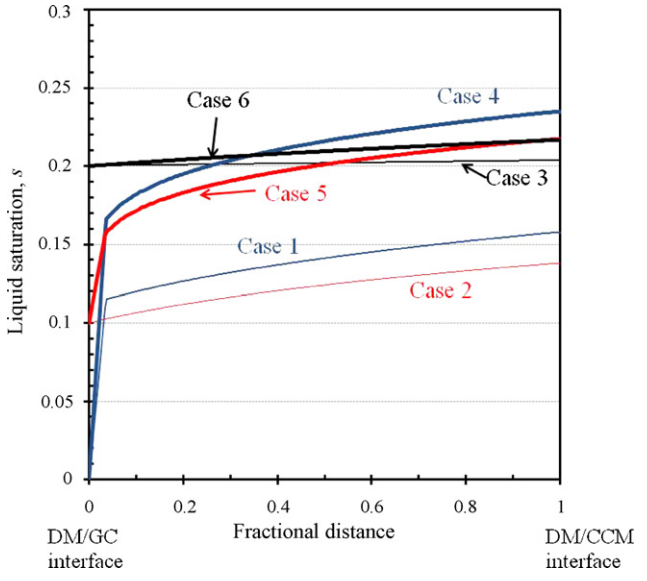

Fig. 5. Liquid saturation profiles in cathode DM with different current density, I, immobile liquid saturation, s_{im}, and interfacial liquid coverage, s_{ic}. Case 1: $I = 1.5$ A cm^{-2}, $s_{im} = 0\%$, and $s_{ic} = 0\%$; case 2: $I = 0.8$ A cm^{-2}, $s_{im} = 0\%$, and $s_{ic} = 10\%$; case 3: $I = 0.4$ A cm^{-2}, $s_{im} = 0\%$, and $s_{ic} = 20\%$; case 4: $I = 1.5$ A cm^{-2}, $s_{im} = 10\%$, and $s_{ic} = 0\%$; case 5: $I = 0.8$ A cm^{-2}, $s_{im} = 10\%$, and $s_{ic} = 10\%$; case 6: $I = 0.4$ A cm^{-2}, $s_{im} = 10\%$, and $s_{ic} = 20\%$. DM contact angle, θ is assumed to be 110° for all cases.

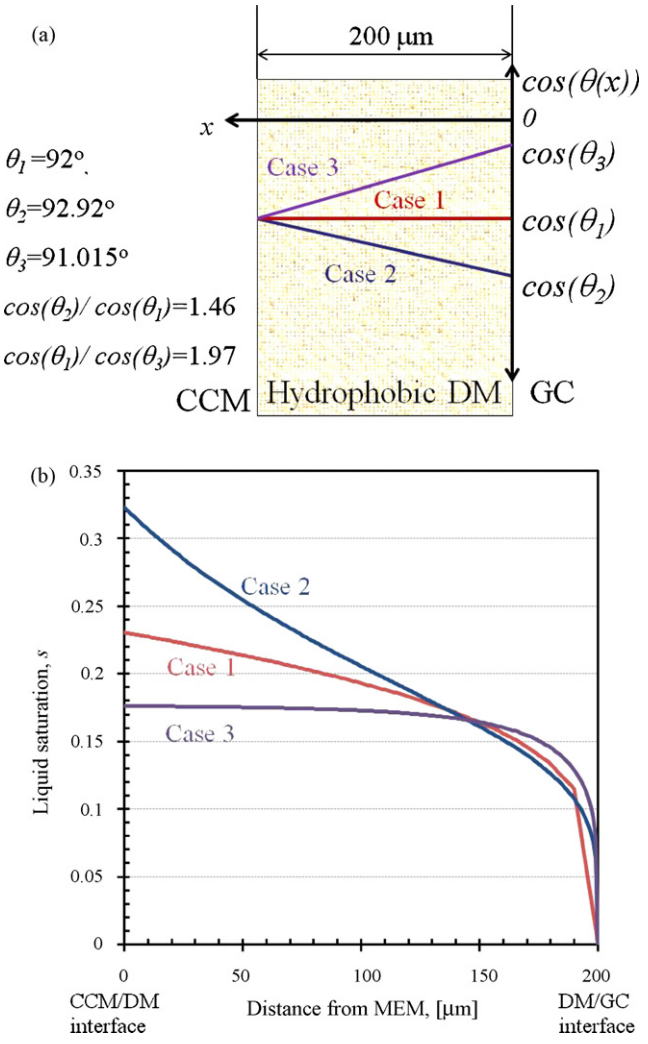

Fig. 6. Liquid saturation profiles in cathode DM with variation of DM contact angle.

sented in Fig. 4 clearly demonstrates that the effect of immobile liquid saturation is less significant with a high level of DM flooding, e.g., the presence of liquid coverage on the DM interfacial surface.

Fig. 5 gives a plot of liquid saturation profiles in the cathode DM at three different current densities, 0.4, 0.8, and 1.5 A cm^{-2}, where a higher value of interfacial coverage is applied to the lower current density cases. Therefore, the assumed values of interfacial coverage at 0.4, 0.8, and 1.5 A cm^{-2} are, respectively, 20, 10, and 0%. The assumption is based on experimental observations that the droplet detachment diameter from the DM interfacial surface is inversely proportional to the air flow velocity in the channels, and thus to the current density under the given air stoichiometry [45]. Two cases are considered for each current density. One is without the effect of immobile liquid saturation (cases 1–3 for $s_{im} = 0.0$) and the other is with consideration of 10% immobile liquid saturation (cases 4–6 for $s_{im} = 0.1$). From a comparison of these cases, it is clearly seen that the effect of immobile liquid saturation is smaller at lower current density. The smallest effect is predicted at 0.4 A cm^{-2}, due to the larger interfacial coverage, i.e., 20%.

It is expected that the wetting characteristics of DM vary spatially due to heterogeneous DM pore structures as well as anomalies in the PTFE treatment of DM. The effects of spatial variation of DM wettability (contact angle, θ) on the liquid water distribution in the DM are investigated in Fig. 6. According to Eq. (3), the capillary pressure P_c is directly proportional to the cosine of the DM contact angle ($\cos\theta$). Therefore, the linear variation of $\cos\theta$ along the DM thickness is considered, as shown schematically in Fig. 6a. Case 1 is a baseline case without variation of $\cos\theta$ (uniform contact angle). The absolute value of $\cos\theta$ linearly increases (case 2) or decreases (case 3) from the CCM|DM interface towards GC, based on the given ratio of $\cos\theta$ in Fig. 6a. Liquid saturation distributions for the three cases are shown in Fig. 6b. It is clearly seen that the direction of contact angle variation along the DM thickness strongly affects both the amount of liquid water accumulation and the shape of the liquid saturation profiles inside the DM. Higher liquid saturation is predicted in case 2 where the DM hydrophobicity increases towards GC. This indicates that liquid water tends to be more easily accumulated in relatively hydrophilic pores rather than being transported towards relatively hydrophobic pores. On the other hand, case 3 has lower liquid water accumulation, because liquid water removal inside the DM is facilitated when the DM hydrophobicity decreases towards GC. The liquid water transport characteristics also influence the shape of the liquid saturation profile in the DM, where the concave-shaped liquid saturation profile for case 2 differs from the convex shape for cases 1 and 3.

4. Conclusions

A one-dimensional, multiphase mixture (M^2)-based fuel cell model has been developed. The model takes into account two key features in order to capture more accurately the accumulation and distribution of liquid water inside DM. The first feature is the effect of immobile liquid saturation, which is a threshold value for continuous liquid phase, and the second feature is the effect of spatial variation of DM wettability, which is mainly caused by the heterogeneity of DM pore structures as well as non-uniform PTFE treatment of DM. One-dimensional PEFC simulations have been performed to investigate these effects on DM liquid water accumulation and flooding. The following conclusions have been reached.

(1) One-dimensional model simulations demonstrate that the effect of immobile liquid saturation is critical. It significantly alters the amount of liquid water accumulation and flooding level in the DM. The effect is diminished, however when the DM faces a high liquid saturation level, particularly with interfacial liquid coverage on the DM surface. Nevertheless, the effect of immobile liquid saturation should be considered in macroscopic two-phase models to understand better the complex water condensation/evaporation processes in the DM and to predict more accurately single- and two-phase regimes of the DM, which are key aspects for the water management of PEFCs.
(2) When linear variation of the cosine of the DM contact angle is assumed along the DM thickness, the model simulations showed that the liquid saturation profiles in the DM are strongly influenced by the direction of the DM contact angle variation. Liquid water transport is enhanced when liquid water is transported from relatively hydrophobic pores towards relatively hydrophilic pores. The numerical observations can impact DM design and optimization strategies for improved water management of PEFCs.

Since these two features are of great importance in DM liquid saturation profiles and flooding phenomena, efforts are currently underway to integrate the present one-dimensional model into a three-dimensional, full-cell PEFC model in order to examine their multi-dimensional effects.

Acknowledgement

Financial support of this work by INHA UNIVERSITY (INHA-37452) is gratefully acknowledged. Thanks are also due to Prof. Chao-Yang Wang at the Pennsylvania State University for useful discussions on the two-phase transport analysis in DM.

References

[1] J.T. Gostick, M.W. Fowler, M.D. Pritzker, M.A. Ioannidis, L.M. Behra, J. Power Sources 162 (2006) 228–238.
[2] E.C. Kumbur, K.V. Sharp, M.M. Mench, J. Electrochem. Soc. 154 (2007) B1295–B1304.
[3] J.T. Gostick, M.W. Fowler, M.A. Ioannidis, M.D. Pritzker, Y.M. Volfkovich, A. Sakars, J. Power Sources 156 (2006) 375–387.
[4] U. Pasaogullari, C.Y. Wang, J. Electrochem. Soc. 151 (3) (2004) A399.
[5] Z.H. Wang, C.Y. Wang, K.S. Chen, J. Power Sources 94 (2001) 40.
[6] D. Natarajan, T.V. Nguyen, J. Electrochem. Soc. 148 (12) (2001) A1324.
[7] S. Mazumder, J.V. Cole, J. Electrochem. Soc. 150 (11) (2003) A1510.
[8] T. Berning, N. Djilali, J. Electrochem. Soc. 150 (12) (2003) A1589.
[9] J. Yuan, B. Sunden, Electrochim. Acta 50 (2004) 677.
[10] G. Lin, W. He, T.V. Nguyen, J. Electrochem. Soc. 151 (12) (2004) A1999.
[11] U. Pasaogullari, C.Y. Wang, J. Electrochem. Soc. 152 (2) (2005) A380.
[12] H. Meng, C.Y. Wang, J. Electrochem. Soc. 152 (9) (2005) A1733–A1741.
[13] C. Ziegler, H.M. Yu, J.O. Schumacher, J. Electrochem. Soc. 152 (8) (2005) A1555.
[14] E. Birgersson, M. Noponen, M. Vynnycky, J. Electrochem. Soc. 152 (5) (2005) A1021.
[15] Y. Wang, C.Y. Wang, J. Electrochem. Soc. 153 (2006) A1193.
[16] H. Ju, G. Luo, C.Y. Wang, J. Electrochem. Soc. 154 (2) (2007) B218–B228.
[17] G. Luo, H. Ju, C.Y. Wang, J. Electrochem. Soc. 154 (3) (2007) B316–B321.
[18] U. Pasaogullari, C.Y. Wang, Electrochim. Acta 49 (2004) 4359.
[19] U. Pasaogullari, C.Y. Wang, K.S. Chen, J. Electrochem. Soc. 152 (8) (2005) A1574.
[20] J.H. Nam, M. Kaviany, Int. J. Heat Mass Transfer 46 (2003) 4595.
[21] A.Z. Weber, J. Newman, J. Electrochem. Soc. 152 (4) (2005) A677.
[22] A.Z. Weber, R.M. Darling, J. Newman, J. Electrochem. Soc. 151 (10) (2004) A1715.
[23] C.S. Kong, D.Y. Kim, H.K. Lee, Y.G. Shul, T.H. Lee, J. Power Sources 108 (2002) 185.
[24] G.G. Park, Y.J. Sohn, T.H. Yang, Y.G. Yoon, W.Y. Lee, C.S. Kim, J. Power Source 131 (2006) 182.
[25] Z. Qi, A. Kaufman, J. Power Sources 109 (2002) 38.
[26] J. Zhang, D. Kramer, R. Shimoi, Y. Ono, E. Lehmann, A. Wokaun, K. Shinohara, G.G. Scherer, Electrochim. Acta 51 (2006) 2715.
[27] J.P. Owejan, T.A. Trabold, D.L. Jacobson, M. Arif, S.G. Kandlikar, Int. J. Hydrogen Energy 32 (2007) 4489–4502.
[28] K. Yoshizawa, K. Ikezoe, Y. Tasaki, D. Kramer, E.H. Lehmann, G.G. Scherer, J. Electrochem. Soc. 155 (2008) B223–B227.
[29] T. Koido, T. Furusawa, K. Moriyama, J. Power Sources 175 (2008) 127–136.
[30] P.K. Sinha, P.P. Mukherjee, C.Y. Wang, J. Mater. Chem. 17 (2007) 3089–3103.
[31] P.K. Sinha, C.Y. Wang, Chem. Eng. Sci. 63 (2008) 1081–1091.
[32] P.K. Sinha, C.Y. Wang, Electrochim. Acta 52 (2007) 7936–7945.
[33] G. Inoue, T. Yoshimoto, Y. Matsukuma, M. Minemoto, J. Power Sources 175 (2008) 145–158.
[34] V.P. Schulz, J. Becker, A. Wiegmann, P.P. Mukherjee, C.Y. Wang, J. Electrochem. Soc. 154 (2007) B419–B426.
[35] C.Y. Wang, P. Cheng, Int. J. Heat Mass Transfer 39 (1996) 3607–3618.
[36] M.C. Leverett, AIME Trans. 142 (1941) 152–168.
[37] K.S. Udell, Int. J. Heat Mass Transfer 28 (1985) 485–495.
[38] E.C. Kumbur, K.V. Sharp, M.M. Mench, J. Electrochem. Soc. 154 (2007) B1305–B1314.
[39] E.C. Kumbur, K.V. Sharp, M.M. Mench, J. Electrochem. Soc. 154 (2007) B1315–B1324.
[40] T. Berning, N. Djilali, J. Electrochem. Soc. 150 (12) (2003) A1589–A1598.
[41] R.E. Meredith, C.W. Tobias, in: C.W. Tobias (Ed.), Advances in Electrochemistry and Electrochemical Engineering, vol. 2, Interscience Publishers, New York, 1962.
[42] T.E. Springer, T.A. Zawodinski, S. Gottesfeld, J. Electrochem. Soc. 136 (1991) 2334–2341.
[43] T.A. Zawodzinski, J. Davey, J. Valerio, S. Gottesfeld, Electrochim. Acta 40 (1995) 297.
[44] S. Motupally, A.J. Becker, J.W. Weidner, J. Electrochem. Soc. 147 (2000) 3171.
[45] F.Y. Zhang, X.G. Wang, C.Y. Wang, J. Electrochem. Soc. 153 (2006) A225–A232.